

### 3. PARTICIPATION IN THE USE OF THE JET FACILITIES BY THE EFDA ASSOCIATES

F. Serra (Head), D. Borba, L. Cupido, M.E. Manso, M.F. Nave, V. Plyusnin, F. Salzedas, C. Silva, D. Alves, P. Belo, R. Coelho, S. Cortes, N. Cruz, B. Gonçalves, L. Meneses, F. Nabais, R. C. Pereira, T. Ribeiro

#### 3.1. INTRODUCTION

The Association EURATOM/IST has proceeded with its participation in the collective use of the JET Facilities by the Associates, in the frame of the “European Fusion Development Agreement” (EFDA) through the “JET Operation Contract” and the “JET Implementing Agreement”.

This chapter presents the main activities carried out during this year in the areas of:

- Operation;
- Scientific exploitation;
- Performance enhancements;
- Management.

#### 3.2. OPERATION

Table 3.1 summarizes the participation of Portuguese staff in the JET Operation Team, through Secondment Agreements with the Association EURATOM/UKAEA.

- Mr. Luis Meneses worked in the Reflectometry and LIDAR Diagnostic Group until October 31<sup>st</sup>. The main activities carried out under the JOC position were:
  - Participation in the upgrade of the X mode correlation reflectometer (kg8b);
  - Operation and maintenance of the O mode fluctuation reflectometer (kg3).
- Mr. Santiago Cortes was in charge of the Motional Stark Effect diagnostic until July 31<sup>st</sup>, including namely:
  - Operation and data analysis of the diagnostic (KS9);
  - Development of a new technique to measure the plasma radial electric field, using the MSE system.
- Dr. Sebastien Hacquin has replaced Mr. Luis Meneses in the reflectometry and LIDAR Diagnostics Group. Besides the activities above mentioned, he has performed the:
  - Development of software to analyse kg8b correlation reflectometry measurements;

#### 3.3. SCIENTIFIC EXPLOITATION

##### 3.3.1. Introduction

The participation in the JET 2002 Work Programme had contributions from twelve scientists to the experimental campaigns C5-C7 at the JET site (Table 3.2), with Dr. Filomena Nave acting as Session Leader in several experiments. The work was focussed on code developments and physics studies related mainly with Task Forces M, D and E.

##### 3.3.2. Work within Task Force M, plus support to S1, S2 and T

###### 3.3.2.1. Comparison of the effects of enhanced radiation on ELM behaviour in JET plasmas

Impurity injection to control the plasma edge conditions has been used in JET ELM-free and ELMy H-mode plasmas. Enhanced radiation decreases the power conducted to the H-mode confinement barrier, thus reducing the edge pedestal temperature, without a large increase in the edge plasma density. A net decrease of the edge pressure at the top of the pedestal is observed leading to kink and ballooning stability. In the ELM-free hot-ion H-mode regime Argon, Xenon and Krypton were injected into the plasma during the heating phase, leading to a delay of the first giant ELM. In JET optimized shear transition to the H-mode can lead to ELM-free periods with edge pedestal pressures and edge MHD activity similar to observations in the ELM-free regime. Puffing either Argon or Krypton has kept the pedestal pressure low, preventing the triggering of type I ELMs. In ELMy steady state plasmas impurity injection can be as effective as Deuterium puffs, to provoke a transition from type I to type III ELMs. This was first observed in Nitrogen and Neon seeded plasmas, with the Mark II divertor. More recently Argon (Figure 3.1) and Neon were used to study

Name	Category	Area	Days
Luis Meneses	Research Assistant	Microwave Diagnostics	308
Santiago Cortes	Research Assistant	Optical Diagnostics	217
Sebastian Hacquin	Assistant Researcher	Microwave Diagnostics	116

Table 3.1 – Portuguese participation in the JET Operation Contract

Name	Competence	1 <sup>st</sup> stay		2 <sup>nd</sup> stay	
		Start	End	Start	End
Filomena Nave	TSL, SL, MHD/AE	04 March	31 May	16 Sep	25 Oct
Paula Belo	IEMHDE, CATS	18 March	25 April	16 Sep	11 Oct
Fernando Nabais	FPE	22 April	17 May	-	-
Francisco Salzedas	MHDME	16 Sep	11 Oct	-	-
Vladislav Plyusnin	MHDME	16 Sep	11 Oct	-	-
Sebastien Hacquin	KG3/KG8B	12 April	15 May	-	-
Carlos Silva	KY3	11 March	27 March	16 Sep	11 Oct
Rui Coelho	SEFDT, NTME	29 April	03 May	-	-
Jorge Ferreira	LHME, PTM	16 Sep	11 Oct	21 Oct	15 Nov
Santiago Cortes	SC/KS9	04 March	17 May	16 Sep	20 Dec
Luis Meneses	KG8B	18 March	11 April	20 May	31 May
Bruno Gonçalves	KY3	16 Sep	11 Oct	04 Nov	15 Nov

Table 3.2 – Portuguese participation in the 2002 JET campaigns

radiative improved plasmas in low and high  $\delta$  configurations. High performance in those discharges is obtained in type I ELM regimes. Impurity seeding reduces the frequency of type I ELMs and in discharges with  $P_{\text{rad}}/P_{\text{tot}} > 70\%$  can lead to intermittent ELM-free periods. However, the ELM amplitude and related power losses are reduced in comparison with non-seeded discharges.

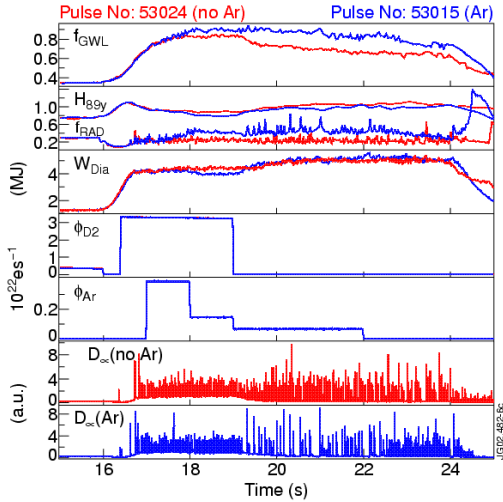


Figure 3.1 - A comparison of discharges with and without Ar. In the after-puff phase lower ELM frequency occurs as the power to the separatrix is reduced.

### 3.3.2.2. Study of the onset of neo-classical tearing modes in JET discharges

The formation of magnetic islands with mode numbers ( $m > 1, n \geq 1$ ) apparently triggered by sawtooth crashes is a concern for ITER operation. The danger these MHD modes pose to future reactor plasmas was seen in the JET DT experiments, where the growth of  $n=3$  and  $n=4$  modes following a sawtooth crash were clearly associated with saturation of the fusion yield.

In recent JET campaigns, the triggering of magnetic islands at different  $\beta$  values and their effect on confinement were extensively studied in ELMy H-mode plasmas designed to study the onset of Neo-classical Tearing Modes (NTM). The possibility that the (3,2) NTMs could be triggered by mode coupling has been assessed both from detailed data-analysis of magnetic pick-up coil signals and from modeling.

Using a large database of NTM observations in a variety of heating configurations, the correlation between NTMs and core MHD activity, such as sawteeth and fishbones, has been studied. Two possibilities were considered: a) The ( $m=3, n=2$ ) driven unstable by toroidal coupling with the  $n=2$  component of the sawtooth precursor; and b) non-linear coupling between three-modes with different toroidal numbers, with the growing ( $m=1, n=1$ ) sawtooth precursor as the main driving mode. Modeling of JET discharges showed that for perfect frequency matching conditions, both toroidal and non-linear coupling may destabilize the ( $m=3, n=2$ ) mode (Figure 3.2). The observed mode frequencies suggest non-linear coupling, to be the most plausible mechanism, with the ( $m=3, n=2$ ) mode being driven by ( $m=1, n=1$ ) and ( $m=4, n=3$ ). In some discharges perfect frequency matching is observed (Figure 3.3). A frequency mismatch on both types of coupling mechanisms considered would introduce a reduction factor for the reconnected flux that is driven by coupling. It is concluded that on average non-linear coupling in JET discharges should be 5-10 times more effective than toroidal coupling in driving significant magnetic reconnection at the  $q=3/2$  surface.

### 3.3.2.3. Study of non-linear coupling using bi-coherence analysis

Bi-coherence is a very useful quantity for the detection of coupling or non-linear interactions between spectral components.

$$b^2(\omega_1, \omega_2) = \frac{\left| \frac{1}{M} \sum_{i=1}^M X^{(i)}(\omega_1) X^{(i)}(\omega_2) X^{(i)*}(\omega_3) \right|}{\sqrt{P(\omega)} \frac{1}{M} \sum_{i=1}^M X^{(i)}(\omega_1) X^{(i)}(\omega_2)} \quad (3.1)$$

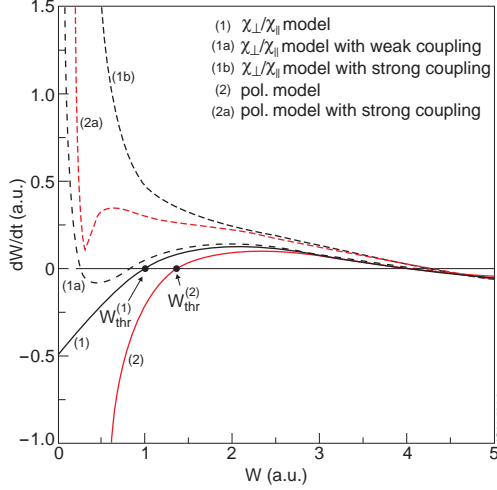


Figure 3.2 – Illustration of the principle of destabilisation of NTMs driven by mode coupling. In the absence of mode coupling effects,  $\chi_{\perp} / \chi_{\parallel}$  and polarization current models yield threshold island widths given by  $W_{thr}^{(1)}$  and  $W_{thr}^{(2)}$ , respectively. When mode-coupling effects are present, the mode starts to grow at a faster pace if the polarization current effects vanish (black dashed curve). If the effect of mode coupling is weak, small saturated states result (black dot-dashed trace for the  $\chi_{\perp} / \chi_{\parallel}$  model

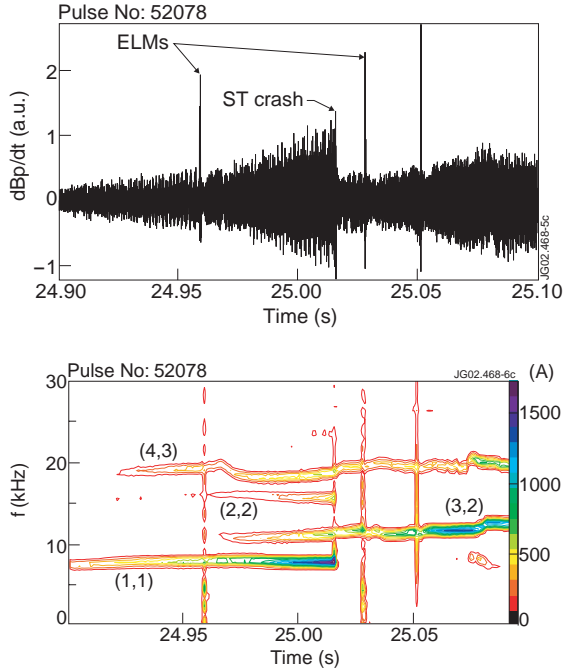


Figure 3.3 - FFT analysis of magnetic signal showing the frequency of modes observed in pulse 52078 around the time a ( $m=3, n=2$ ) mode started to grow. The following MHD modes are observed: sawtooth (1,1) and (2,2) precursors, a (4,3) mode unaffected by the sawtooth crash (at  $t=25.03s$ ) and the onset of a (3,2) mode observed above the noise level at  $t \approx 24.965s$ , around the time the (4,3) frequency is observed to decrease.

When averaged over different realizations, this value is different from zero when the condition

$$\omega_1 + \omega_2 = \omega_3 \quad \text{and} \quad \phi_1 + \phi_2 = \phi_3 + \text{const.} \quad (3.2)$$

is verified throughout the analyzed signal. This analysis method is well suited for the study of non-linear coupling three-wave mode coupling and has therefore been applied to the analysis of magnetic signals showing NTMs. The study has been divided in two parts concerning the analysis of NTM onset and of NTM islands.

The bi-coherence method of several discharges, reveals the existence of non-linear mode-coupling between (1,1), (4,3) and (3,2) modes at the onset of the (3,2) NTM before the sawtooth crash. This result confirms a model for NTM trigger previously proposed in a work of collaboration between CFN and CNR-Milan.

Analysis during the NTM saturated phase of a (3,2) NTM has also been done for one JET discharge. It finds a strong coherence between (1,1), (4,3) and (3,2) modes (Figure 3.4), suggesting that non-linear coupling at the later stage of the NTM may be responsible for the observed amplitude reduction in some discharges<sup>1</sup>.

#### 3.3.2.4. Time-frequency analysis of non-stationary signals in fusion plasmas using the Choi-Williams distribution

Fusion plasma signals, such as magnetic ones, often contain information on non-stationary phenomena and therefore have time-varying spectra. The tools usually employed to analyze such signals, amongst which the spectrogram based on the short-time Fourier transform is dominant, are severely limited by a trade-off between time and frequency resolutions. Signal processing techniques based on the Wigner and related time-frequency have been used to overcome this shortcoming in areas of research such as geophysical exploration, natural sciences, and several others.

Particularly, the Wigner distribution has been applied to the measurement of electron density profiles in tokamak plasmas through broad-band microwave reflectometry. However, despite its ability to follow instantaneously even the fastest changing spectra, the use of the Wigner distribution can be hindered by the existence of artifacts in the time-frequency plane. Such artifacts appear whenever signals have multiple components, which interfere and originate cross terms. They are notorious for making the interpretation of the time-frequency plane difficult, except for signals having but a few clearly distinguishable components. Therefore, to deal with multi-component signals, a tool is required that, besides providing good time and frequency resolutions, can further yield a clear picture of the time-frequency plane. The Choi-Williams distribution is one

<sup>1</sup> This work was done in support of an experimental proposal for JET TFM (campaign C7) by members of IPP.

such tool, a so-called reduced interference distribution that gradually deviates from the Wigner distribution. It increasingly reduces artifacts by decreasing their magnitude and spreading them throughout the time–frequency plane.

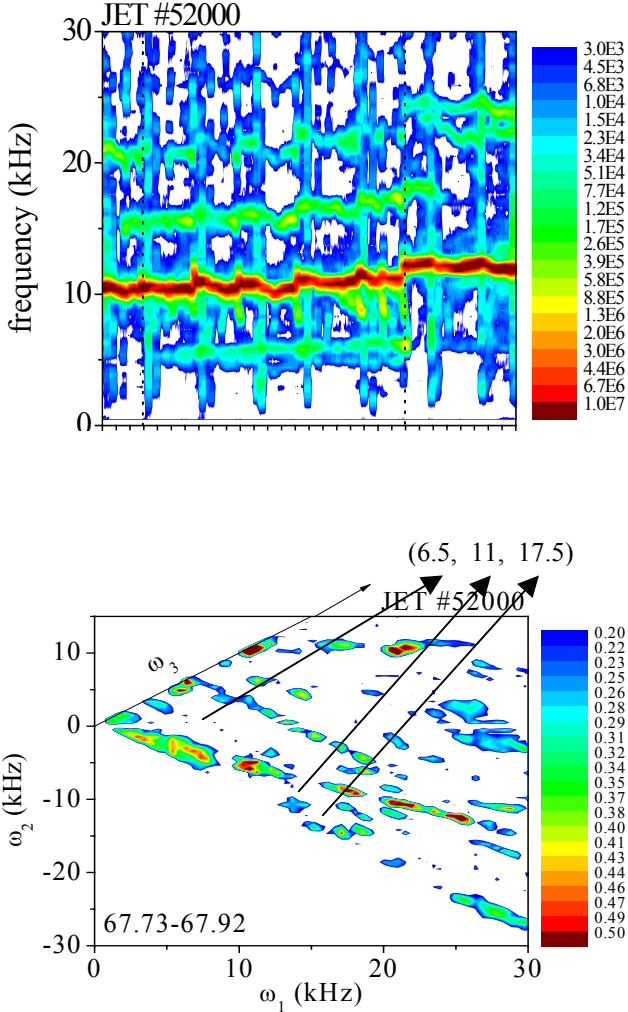


Figure 3.4 a) FFT analysis of magnetic pick-up coil showing frequency evolution of MHD modes: (1,1) mode with frequency ~6 kHz, (3,2) mode with frequency ~11 kHz and (4,3) mode with  $f \sim 17$  kHz); b) Bi-coherency analysis for the same magnetic signal

Its good time–frequency resolution makes the Choi-Williams distribution an useful tool to, for instance, identify precursors of fast magnetohydrodynamic (MHD) instabilities, such as edge localized modes (ELM) and sawtooth crashes. Here, we look at the time of onset of neoclassical tearing modes (NTM) with respect to a sawtooth crash. MHD mode analysis using techniques based on the short-time Fourier transform shows that, for JET pulses with large neutral beam injection (NBI) powers, the (3,2) NTM typically start around 20 ms to 200 ms before a sawtooth crash. This raises the possibility that NTM could be triggered by mode coupling with sawtooth

precursor components. However, it has not been possible to resolve the time of the NTM onset with respect to sawtooth in discharges with low NBI (less than 5 MW) and ion cyclotron resonance heating (ICRH), giving the impression that in these cases with low plasma rotation, the NTM started with, or after the sawtooth crash.

The objective of using the Choi-Williams distribution in this case is therefore to find out whether the NTM that are clearly observed to grow after the sawtooth crash, started before, after, or simultaneously with the sawtooth, which requires both a high time resolution and a low level of artifacts. Figure 3.5 clearly shows, thanks to the significant reduction of artifacts, that modes such as the one around 5.0 kHz appear about 3 ms before the sawtooth. This conclusion could not have been achieved using the spectrogram, since the region around the sawtooth event would be blurred, and decreasing the window size in order to improve the time resolution would yield a poor time–frequency representation, with insufficient frequency resolution.

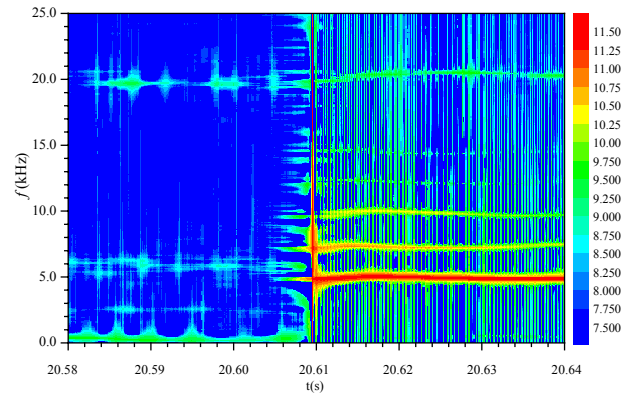


Figure 3.5 - Logarithmic representation of the Choi-Williams distribution of a magnetic activity signal from the JET tokamak (pulse 50668, node DI/C3-CATS<C:003).

### 3.3.2.5. Use of TRANSP for transport analysis of the radiative improved confinement H-mode

TRANSP, a tokamak core transport and modeling code specially tuned for data analysis, is almost certainly the best available tool for interpretative transport analysis. TRANSP code is very computing time consuming because emphasis is given on accuracy and not necessarily on speed however multiple alternative models are offered allowing a speed/accuracy tradeoff. Part of the current research done by TRANSP team is to develop new models to address hot research topics current under investigation and recently to have some predictive analysis capability. Some effort must address in future the reduction of the computing time by code optimizations.

Some tools are being developed in Interactive Data Language (IDL) to simplify and reduce the time spent in analyzing and preparing input experimental data as well

as the visualization of the results for a typical TRANSP simulation. A graphical tool was developed to read experimental data obtained by several JET diagnostics through the newly installed MDS+ data acquisition and analysis system, to visualize this data interactively and ultimately to process data from several different diagnostics to construct, for example, a consistent evolution of the temperature and density profiles for electrons and ions.

Figure 3.6 shows the ion temperature profile for a time slice which is reconstructed from the core and edge charge exchange spectroscopy data (CXSM, CXSE). Figure 3.7 presents the plot of the electron temperature reconstructed from the electron cyclotron emission radiometer and extended to the edge and core of the plasma using Thomson scattering measurements. Other quantities are also processed like the effective ionic charge or the toroidal angular frequency.

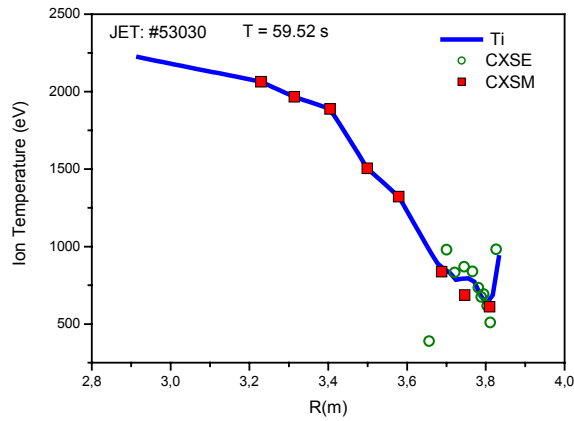


Figure 3.6 - Reconstructed ion temperature profile ( $T_i$ ) from core/edge charge exchange spectroscopy data (CXSM/E)

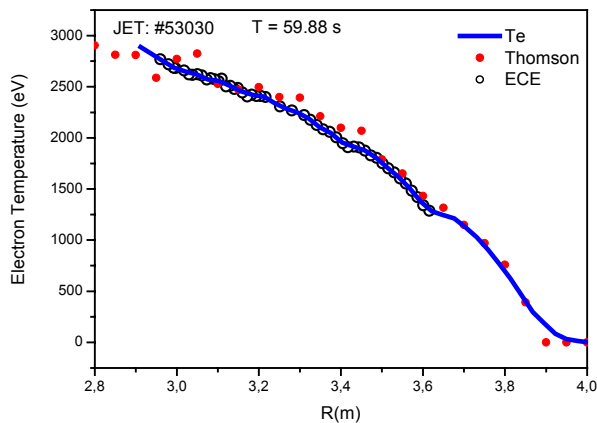


Figure 3.7 - Reconstructed electron temperature from electron cyclotron emission radiometer and Thomson scattering measurements

A graphical tool is also being developed to visualize and check the accuracy of the numerical simulation. This tool reads directly from the multidimensional output file generated by TRANSP using the common data format.

These tools will simplify the transport studies planned for the near future namely for the Radiative Improved (RI) confinement H-mode experiments (with radiating mantles showing simultaneously high confinement and high density at high radiation levels).

### 3.3.2.6. Study of the effect of plasma shape on the TAE stability

The effect of the plasma shape on the TAE stability in conventional scenarios was studied in recent experiments by measuring the AE excitation threshold, using the drive provided by resonant NBI ions.

Plasmas with limiter and X-point configurations were compared. The results showed that 30% less NBI power was required to destabilise TAEs with intermediate toroidal mode numbers in the limiter configuration, ( $P_{NBI}=5.3\text{MW}$  in limiter configuration compared to  $P_{NBI}=8\text{MW}$  in X-point configuration) and further away from the resonance ( $V_{||}(NBI)\approx 0.8 V_A$  compared to  $V_{||}(NBI)\approx 0.95V_A$  due to different plasma densities). This result confirms earlier predictions and measurements of the stabilising effect of the x-point on TAEs, in plasmas with monotonic q-profiles. As expected, this effect appears to be weaker for radially localised  $n=5\div 7$  TAEs than for global  $n=1\div 2$  TAEs (Figure 3.8).

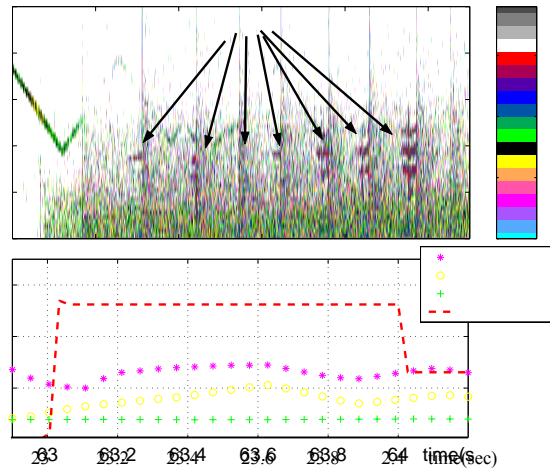


Figure 3.8 - Limiter plasma with monotonic q-profile:  $n=5\div 7$  TAEs become unstable at  $P_{NBI}=5.3\text{MW}$ .

### 3.3.2.7. Analysis of the Alfvén cascades instabilities

Further analysis of the Alfvén cascades instabilities in optimised shear plasmas, which are linked to integer

values of the  $q$  profile, have showed that the occurrence of these instabilities are also linked with some transport events that lead to an ITB formation. It seems to be unlikely that the Alfvén cascades themselves directly triggers the ITB event since the correlation between  $q_{\min}$  reaching an integer value and the ITB triggering events were earlier identified in plasmas without ICRH and without Alfvén cascades. However, Alfvén cascades can be used as a diagnostic tool for identifying the ITB triggering events on an inter-shot time interval with the aim of adjusting the input power timing and the plasma parameters for a more successful ITB scenario.

### 3.3.2.8. Numerical analysis of the loss of sawtooth stabilisation by ICRH driven fast particles in low density discharges

The fast particles generated by Ion Cyclotron Resonant Heating (ICRH) are known to have a significant influence over the sawtooth stability. Normally these particles have a strong stabilising effect and lead to the appearance of long sawtooth periods, known in the literature as monster sawtooth.

In JET ICRH-only experiments where low densities plasmas were used, it was found that when the density decreases below a certain threshold, monster sawteeth disappear and were replaced by the short period sawteeth commonly found in discharges without ICRH. This suggests that the ICRH driven fast particles may somehow lose its stabilising effect over the internal kink mode responsible by the sawtooth activity when the plasma density is sufficiently low. This possibility was analysed using the CASTOR-K code, a gyrokinetic code that calculates the transference of energy between the internal kink mode and the ICRH driven fast particles population.

Giant sawteeth can be observed in pulse #47576 after  $t=51.6$  s, when the plasma central density increases approximately above  $n_e \approx 2.0 \times 10^{19} \text{ m}^{-3}$  (Figure 3.9). In the higher density discharge, monster sawteeth are present since the beginning of the heating phase, which is consistent with the fact that during this period the density in this discharge was maintained over  $2.0 \times 10^{19} \text{ m}^{-3}$ . Since the only relevant difference in these discharges was the central electron density  $n_e$ , one can expect the change in sawtooth behaviour to be related to the plasma density.

Equilibrium for both discharges and for several time instants were calculated with the HELENA and EFIT codes and no significant differences were found. In particular, similar profiles of the safety factor were found. The eigenmodes calculated with the MISHKA code were also identical, what suggests that the observed differences in the sawtooth behaviour must be related with changes in the fast particles distribution. In fact, classical slowing down time of fast ions is inversely proportional to the plasma density, so one would expect lower density plasmas to have higher fast ions temperatures. It is known that high energy particles have non-standard orbits whose width normally

increases with the energy. When the width of the orbits reaches the size of the  $q=1$  surface, the stabilising effect is expected to be lost. Then, one can predict that at some size a rapid decrease in the fast particles stabilisation term  $\gamma_{\text{HOT}}$  ( $\gamma = \gamma_{\text{MHD}} + \gamma_{\text{HOT}}$ ) must occur when increasing  $T_{\text{HOT}}$ . To confirm this, the perturbation on the mode growth rate due to the interaction with the fast particles,  $\gamma_{\text{HOT}}$ , was calculated using the CASTOR-K code (Figure 3.10).

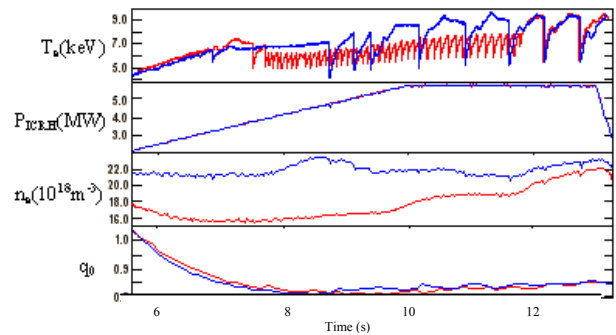


Figure 3.9 - Temporal evolution of the electronic temperature, ICRH power, electronic density and safety factor on the axis during pulses #47575 (blue) and #47576 (red).

Figure 3.10 - Perturbation on the internal kink mode growth rate  $\gamma_{\text{HOT}}$  as function of the fast ions temperature  $T_{\text{HOT}}$ .

So, CASTOR-K results would be consistent with experimental data if, the transition between the regime of short sawteeth period and the regime of monster sawteeth occur somewhere below  $T_{\text{HOT}} \sim 2$  MeV approximately. In other words, they would be consistent if the threshold in density of  $n_e \approx 2.0 \times 10^{19} \text{ m}^{-3}$  corresponds to a threshold in the fast ions temperature somewhere below  $T_{\text{HOT}} \sim 2$  MeV. To verify this, the temporal evolution of  $T_{\text{HOT}}$  is required. Unfortunately the knowledge of  $T_{\text{HOT}}$ , which is calculated with data from the PION code, is not very

accurate. It is known the calculation produce overestimated values, but not by how much. Figure 3.11 shows the temporal evolution of  $T_{HOT}$  for pulses #47575 and #47576, calculated with data from the PION code.

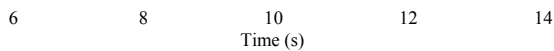


Figure 3.11 - The temporal evolution of  $T_{HOT}$  for pulses #47576 (solid line) and #47575 (dashed line).

The first slight increase in the sawtooth period in #47576 (Figure 3.9) occurs at  $t=10$  s approximately. This corresponds to a decrease in the fast ions temperature to  $\sim 2$  MeV (Figure 3.11) that is the value for which the stabilising effect of ICRH driven fast particles start rising (Figure 3.10). Monster sawteeth appear around  $t=12$  s, when the plasma density increases above  $n_e \approx 2.0 \times 10^{19} \text{ m}^{-3}$  and a decrease in the fast ions temperature from 2 MeV to 1.5 MeV is observed. It is not possible to establish a more accurate threshold in  $T_{HOT}$ , but it appears to be in the range predicted by the code CASTOR-K. Thus, one can conclude that the disappearance of monster sawteeth in low density plasmas is likely to be caused by a loss of stabilisation of the ICRH driven fast particles due to an increase in its temperature. The threshold for the transition to the monster sawteeth regime is approximately  $n_e = 2.0 \times 10^{19} \text{ m}^{-3}$  in terms of the plasma density and roughly  $T_{HOT} \approx 1.5$  MeV in terms of fast ions temperature.

### 3.3.2.9. Study of the physical mechanism of the fast destruction of energy confinement that triggers major density limit disruptions

Studies of the physical mechanism of the fast destruction of energy confinement that triggers major density limit disruptions at JET and ASDEX Upgrade started at the beginning of 2002.

The experiments in JET carried out during campaign C6 seem to be in good agreement with the experiments of both ASDEX Upgrade and RTP. The observed temperature erosion is also observed to initiate at the O point of the (2,1) mode, advancing afterwards to the plasma core.

The spectrogram in Figure 3.12 shows an abrupt increase in the frequency of density fluctuations coinciding with the onset of the  $T_e$  erosion in the region of the  $q=2$  rational surface. This abrupt increase in fluctuations frequency is consistent with the sharp increases in the  $n_e$  profiles observed at ASDEX during the same phase. Since these changes in density precede the erosion of the temperature profile, they indicate that mixing of cold plasma with hot plasma in this region is the cause of the  $T_e$  erosion. It should also be noted that an intense peak of electron cyclotron emission, observed in RTP tokamak after the flattening of the  $T_e$  profile during the energy quench was observed in JET disruptions.

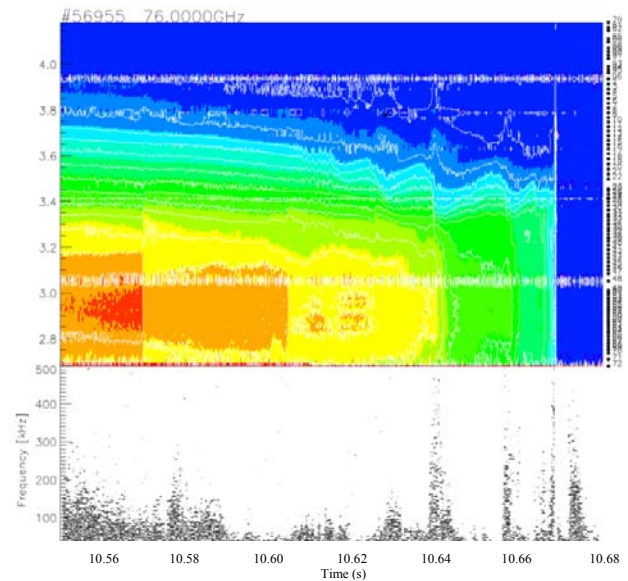


Figure 3.12 – JET density limit disruption in a D plasma, provoked by Ne gas-puff. Above, electron temperature evolution measured with an ECE. Below, spectrogram of density fluctuations probed at 76 GHz. The position (3.8 m) of the cut-off layer deduced from a LIDAR  $n_e$  profile at  $\sim 10.63$  s is indicated by a \* on the picture above. Notice the correlation between the abrupt increase in frequency and the  $T_e$  erosion. At  $\sim 3.7$  m,  $\sim 10.67$  s is visible an intense peak in ECE.

### 3.3.2.10. Study of runaway electrons in JET disruptions

#### A. Analysis of experimental data

Existing experimental data on runaway electrons generated during disruptions was added by that obtained in the Campaign C6. The density limit disruptions were initiated by massive Argon and Neon puffs into JET discharges. Characteristics of the runaway electrons generated during disruptions were studied. Several disruptions revealed the existence of the runaway electron current plateau with values up to 1 MA (Figure 3.13).

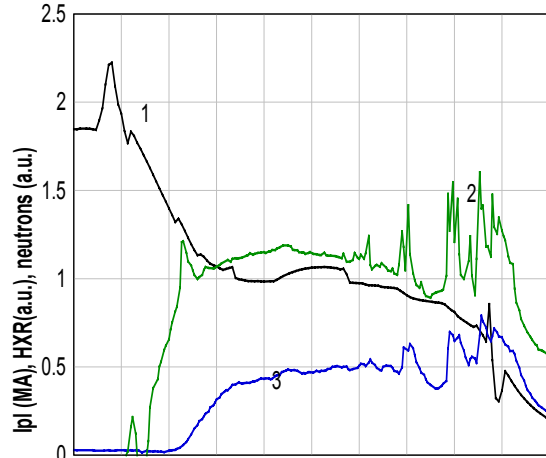


Figure 3.13. Runaway electron generation in disruption in the pulse #56953. Temporal evolution of the plasma current (curve 1), hard X-ray (curve 2) and neutron emission (curve 3) is presented

Runaway electron beams produced observable soft X-ray image by excitation of plasma impurity ions. The analysis of the beam image allowed determining the beam spatial structure and its temporal evolution. Appearance of the low energy runaway electrons is observed in soft X-ray emission. Detailed analysis of the runaway electron characteristic allows the conclusion that substantial population of the low energy runaway electrons exists already at the beginning of the current quench stage (Figure 14). As the runaway electrons gain more energy before current quench starts, the soft X-rays become a consequence of the interaction of the runaway beam with the surrounding surfaces of the device. There is clear coincidence between the bursts of the hard X-ray and neutron emissions, and appearance of the soft X-rays when runaway beam hits the wall. These observations are in adequate agreement with the results of the numerical modelling of the runaway generation process at the thermal quench stage of the disruption.

#### B. Modelling of thermal quench and runaway generation

The main mechanism responsible for the runaway production in disruptions is considered to be an avalanching of the high-energy electrons due to close electron-electron collisions between existing runaway and thermal electrons. The secondary avalanching is not possible without the primary generated runaways that can exist in the pre-disruptive plasma, or they can be produced during the thermal quench. Thermal quench still is the most unknown transient stage since the strong plasma perturbations do not allow measuring in detail the plasma

parameters evolution. Meanwhile, the large increase of the electric field in plasma due to electron temperature decrease should be expected during the quench. This should lead to the noticeable generation of super-thermal or runaway electrons.

Runaway electrons can also be generated during the magnetic reconnection at the pre-disruption stage due to local electric fields increase. The sequence of very complicated transient events during disruption does not allow reliable extrapolation of the present time results on disruption-generated runaways for the ITER case. Experimental data on disruptions makes possible only to estimate and extrapolate the duration of different stages of the disruption, usually distinguished as several steps of the thermal quench. Characteristic times of these stages are the delay time between first temperature decrease ( $T_e \sim 1$  keV) and complete quench, and duration of the fast thermal collapse (usually  $\sim 100$ - $500$   $\mu$ s).

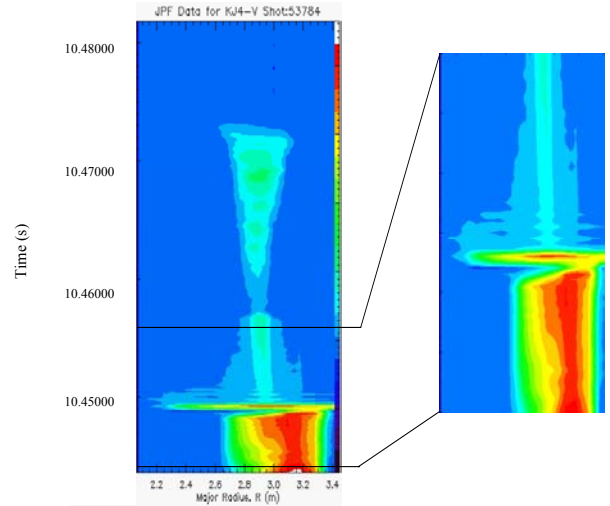


Figure 3.14. Soft X-ray image of the disruption in pulse #53784.

Calculations performed in terms of a simple model (single test particle acceleration and 0-D calculations of the runaway density) predict a strong increase of the longitudinal electric field and the creation of the RA electrons with substantial energy and density due to the Dreicer mechanism for the case of 1 keV thermal quench in a large-scale tokamak ( $a_{p1}=1$ - $1.2$  m,  $2$  MA  $< I_{pl} < 6$  MA,  $\langle n_e \rangle = 10^{20}$  m $^{-3}$  and temperature decay within  $\sim 100$ - $500$   $\mu$ s). Analysis of calculation results shows that RA electrons increase their energy and density mainly during the stage when electron temperature decreases below 100 eV. Duration of this phase has to be considered as the most critical parameter, since even for  $\tau_{fast} \sim 200$   $\mu$ s, the energy of the runaways can achieve up to 7-10 MeV at a density of  $\sim 10^{11}$ - $10^{12}$  m $^{-3}$ .

Creation of runaways with such parameters obviously can cause the process of secondary runaway electrons avalanche, which leads to abrupt increase of the runaway

electrons density at the energy  $\geq 10$  MeV. Calculations performed for the different values of the fast quench ( $\tau_{fast}$ ) in medium and large tokamak experiments show that in medium scale tokamaks (TEXTOR, ASDEX-Upgrade) the duration of the thermal quench and evolution of plasma parameters during disruption don't allow significant runaway generation (Figure 3.15). Meanwhile, calculations performed for ITER ( $I_{pl} = 24$  MA and  $\tau_{fast} = 1$  ms) predicts very large runaway electron density produced before avalanching starts.

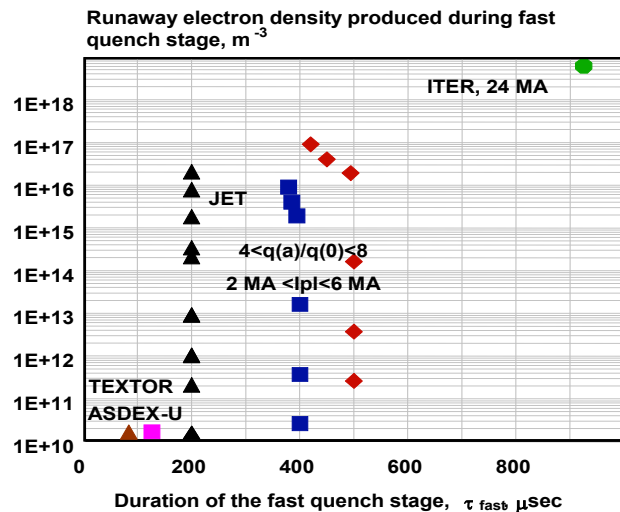


Figure 3.15 - The runaway generation in the thermal quench without inclusion of the secondary avalanching (upper values of the runaway density are pre-avalanche values for JET and ITER)

Taking into account these results the experimental facts, that disruptions with runaways not always observed in JET even in similarly disrupted discharges, small quantity of runaway disruptions were observed in TEXTOR and ASDEX-Upgrade can be plausibly explained, at least in the frames of the following model. This model establishes the correlation between efficiency of the primary generation mechanism on the stage of electron temperature drop and consequent appearance of conditions for further runaway generation including the secondary avalanche during disruption. On the other hand, if the density of runaway will exceed certain threshold, the appearance of instability can stop the acceleration process serving like mitigating mechanism.

### 3.3.3. Work within Task Force D

#### 3.3.3.1 Direct measurements of the radial electric field using the upgraded MSE diagnostic

In 2002, the main task was to control the diagnostic and analyze the data produced by the motional Stark effect (MSE) diagnostic. A new technique to measure the plasma

radial electric was also developed. This technique consists in firing sequentially two neutral beam injectors at different energies. The change in the polarization angle of the MSE emission encodes the measurement of  $E_r$ . Experimental results for the case of little plasma rotation have shown the feasibility of this technique. The radial profiles of  $E_r$  show a global decrease after the high power phase (Figure 3.16). It can also be noticed a near zero electric field near the magnetic axis ( $R_m \sim 3.1$  m).

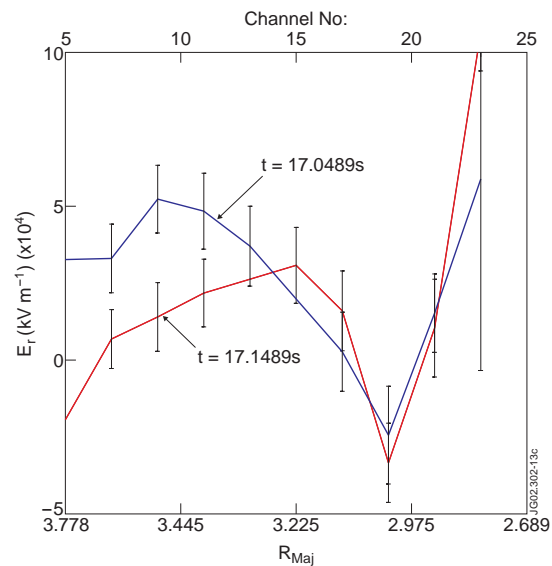


Figure 3.16 - Radial profiles of  $E_r$

Systematic analysis of JET extreme reversed shear (ERS) discharges using EFIT with MSE constrain and high order polynomials to fit the experimental data have been done, aiming to investigate the performance of the equilibrium reconstructions in cases where the so-called *current hole* is present. The *current hole* is a region near the magnetic axis where the current density is nearly zero. Current is excluded from this central region and instead flows in a narrow skin at its boundary. An electron ITB is often observed with steep gradients in  $T_e$  near the position of the current skin. In all these discharges sawtooth-like events characterized by periodic collapses in the electron temperature  $T_e$ , despite  $q(r)$  well above unity everywhere. Those crashes clearly interferes with the MSE signals.

Using a non-perturbative technique in solving the Grad-Shafranov equation, i.e. keeping magnetic data the same before and after the crash, equilibrium reconstruction results have shown that temperature crashes are playing a major role in the current density rearrangement scheme. Moreover, it seems that they are likely contributing to global broadening of the current skin and to shrinking of the current hole leading to its degradation (Figure 3.17).

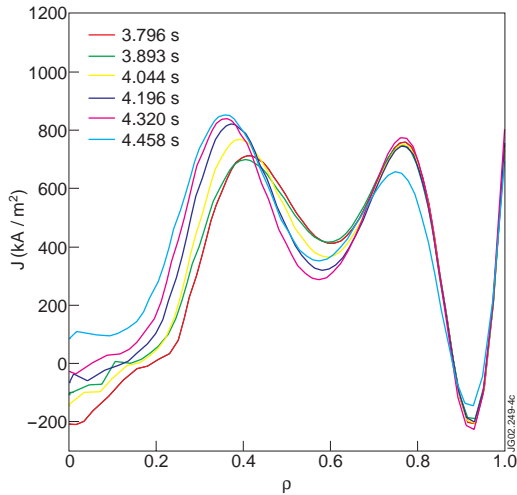


Figure 3.17 - Current density time evolution between crashes showing the shrinking of the current hole and broadening of the current skin.

### 3.3.3.2. Turbulence studies with the upgraded correlation reflectometer

A better understanding of the relationship between turbulence and transport in the core of JET plasmas can be provided by the measurement of the radial correlation length of the plasma fluctuations, with good spatial and temporal resolution, by the upgraded X-mode reflectometer<sup>2</sup>.

Preliminary results obtained during recent JET experiments, keeping constant one frequency and varying the other in four steps (Table 3.3), show some interesting correlation results during the H mode plasmas. Figures 3.18 and 3.19 present respectively the flux lines, and the cut-off at 20 s and 22 s, in which the reflectometer measured just before the L-H transition ( $t=20.4$  s (Figure 3.20) and during the ELMy H mode (Figure 3.21). The correlation coefficient increases close to the H mode transition, but is 0 during the L phase, the next measurement is during the ELMy phase and the correlation coefficient is around 0.5, decreasing during the ELM.

The reflectometer can also be used to study density fluctuations. Figure 3.22 shows a spectrogram of step frequency source of the 76-78 GHz system during ELMs.

Step	Frequency Difference [MHz]			
	76-78 GHz	85-87 GHz	92-96 GHz	100-1006 GHz
0	600	300	0	-2800
1	900	600	250	-2400
2	1200	900	750	-1900
3	1700	1200	1200	-1400

Table 3.3 – Operation frequency in pulse # 56793

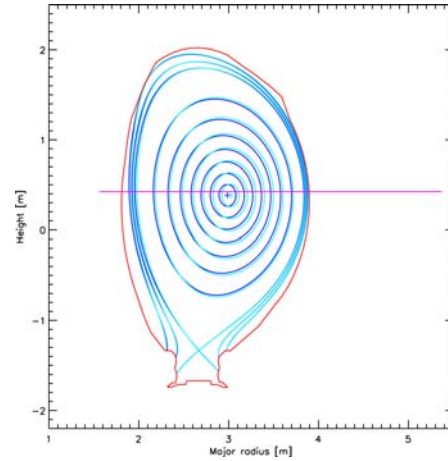


Figure 3.18 – Plasma magnetic configuration

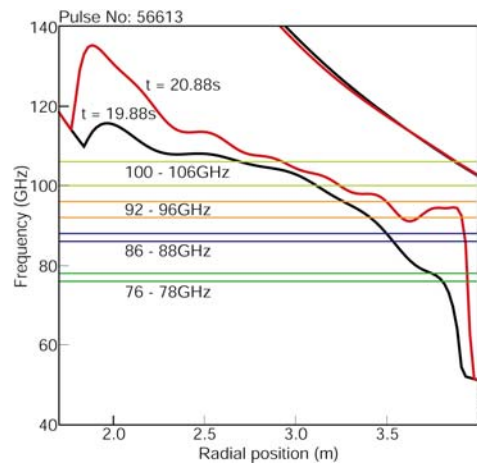


Figure 3.19 – Cut-off position

### 3.3.4. Work within Task Force E

#### 3.3.4.1. Interplay between parallel transport and poloidal flows

A. Study of the link between parallel flows and poloidal flows in the proximity of the LCFS.

It has been observed in the Alcator C-mod SOL that the poloidal velocity cancels the poloidal component of the parallel velocity so that the total flow is mainly toroidal. Figure 3.23 shows that this is not the case in the JET SOL where the poloidal component of the parallel velocity is much larger than the poloidal velocity. Only inside the separatrix the poloidal flow compensates part of the parallel flow. This behaviour is explained by the flat profiles of floating potential and temperature resulting therefore in small radial electric fields. This result has important consequences for the transport of impurities in the SOL and for the deposition of carbon and tritium in the divertor region.

<sup>2</sup> Section 3.4.2.

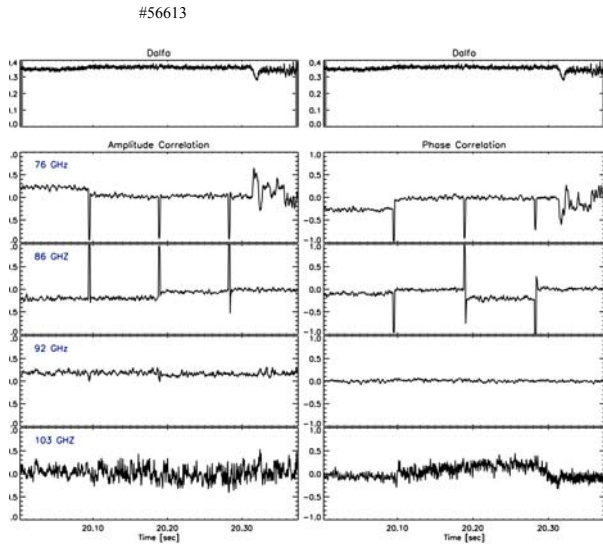


Figure 3.20 – Corr. Coeff. L mode

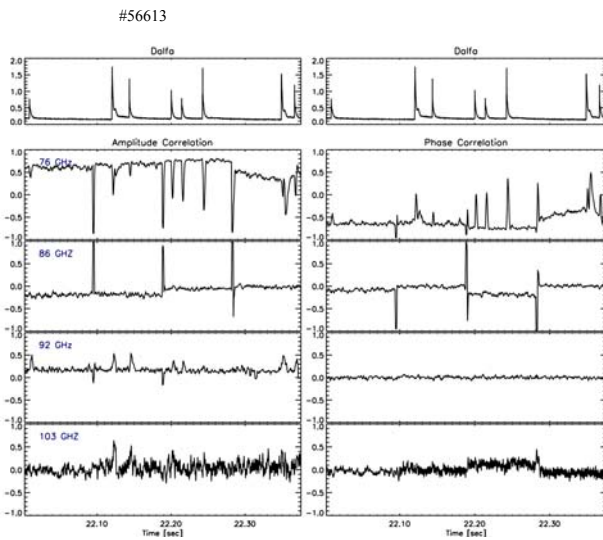


Figure 3.21 – Corr. Coeff. ELM H mode

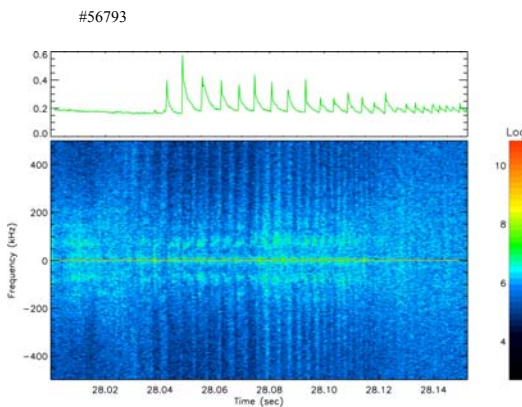


Figure 3.22 - spectrogram during the ELM phase on the edge channel

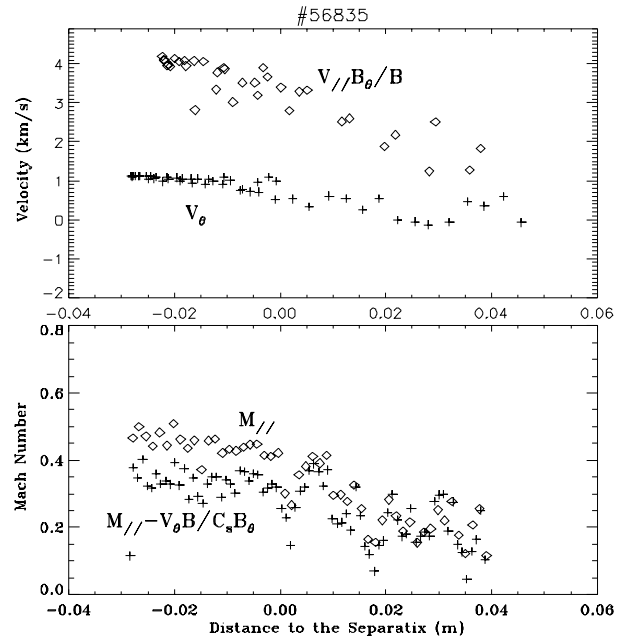


Figure 3.23 – Radial profile of the poloidal velocity and the poloidal projection of the parallel flow

B. Study the dynamical coupling between parallel-poloidal flows and turbulent transport. Measured parallel Mach numbers (0.3-0.8) are much larger than those expected from fluid simulations (0.1-0.2). A possible explanation is that parallel Mach numbers are dynamically linked with the size of turbulent transport events. This result implies that the Mach number is partially dominated by turbulent mechanisms explaining the disagreement with non-turbulent models.

Figure 3.24 shows the expected value of the parallel Mach number for a given turbulent transport in the Scrape-of-Layer region ( $r-r_{LCFS} = 0.5 - 2$  cm). The results show that turbulent transport and parallel flows are dynamically coupled. The expected value of parallel flows significantly increases as the size ExB turbulent transport events gradient increases. The most probable value of the Mach number are close to the predicted by fluid codes, however there are large amplitude turbulent events that increase the Mach number and that physics is not included in fluid codes.

The interplay between the statistical properties of turbulent transport and parallel flows has also been investigated at different time scales. The shape of PDFs of transport is significantly modified as the averaging parameter ( $\Delta N$ ) increases: negative transport events are reduced and the shape of the tail of the distribution changes in agreement with previous observations. At time scale decreases (e.g.  $\Delta N$  increases) the PDF of transport is mainly dominated by outwards transport events and the dynamical coupling between transport and parallel flows becomes stronger. This result suggests that low

frequencies have a dominant effect on the link between parallel flows and turbulent transport.

On the basis of the present results, and considering previous observation in the SOL region of the JET tokamak, we have to conclude that the bursty and strongly non-gaussian behaviour of turbulent transport is strongly coupled with fluctuations in gradients and parallel flows. This dynamical coupling reflects that parallel flows are, at least partially, by turbulence mechanisms. This observation is consistent with recent models, which have pointed out the role of turbulence on toroidal momentum transport to explain the onset of spontaneous rotation in tokamak plasmas.

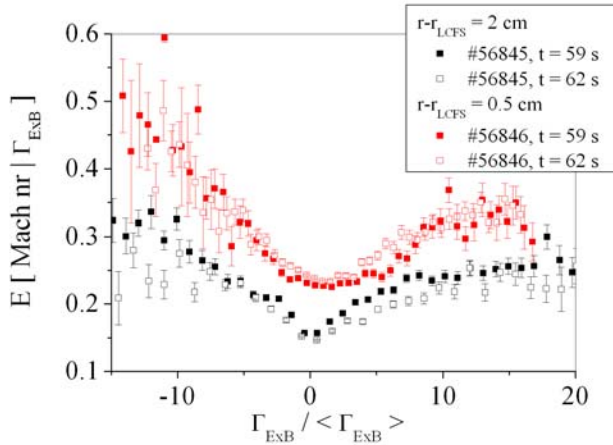


Figure 3.24 - Expected number of the parallel Mach number versus local turbulent transport

Considering that significant plasma turbulence has been observed both in the edge and core plasma regions in fusion plasmas, the present results might have a strong impact in our understanding of parallel momentum transport in fusion plasmas. Particularly interesting will be to investigate the link between magnetic topology (i.e. rational surfaces) and parallel flows driven by turbulence. Because fluctuations are expected to show maximum amplitude at the rational surface, a significant radial variation in the magnitude of parallel flows would be expected on the basis of the results reported in this paper. This mechanism can provide sheared parallel flows linked to the location of rational surfaces which could be an ingredient to explain the spontaneous formation of transport barriers near rational surfaces in fusion plasmas.

### 3.3.4.2. Edge Localized Modes propagation and fluctuations in the JET SOL region

The possible link between the amplitude and the radial propagation of ELMs might have an important consequence in the extrapolation of ELMs impact on the divertor plates of future devices. Perturbations in ion saturation current and potential signals induced by the appearance of ELMs are

observed up to 7 cm beyond the LCFS. This result implies that the ELMs convective SOL-width is much broader than the typical SOL-width measured during time intervals between ELMs.

The propagation of fluctuations has been investigated measuring the ELM arrival time at two probes radially separated. Typical time delays are in the range of 2 - 10 ms for sensors radially separated by 0.5 cm. This implies a radial velocity in the range of 1000 m/s. Figure 3.25a shows the expected value of the radial effective velocity versus fluctuations in the radial gradient ( $\nabla \tilde{I}_s$ ). Radial effective velocities increase up to 2000 m/s during ELMs. This radial velocity is consistent with the  $E_{\theta} \times B$  velocity, which can be computed from the poloidal electric field shown in Figure 3.25b. The present experimental results suggest that the radial velocity of ELMs increases with the ELM size (i.e. increasing  $\nabla \tilde{I}_s$ ). Large transport events seem to have also an associated poloidal velocity, computed from the  $E_r \times B$  velocity ( $E_r$  being the radial electric field).

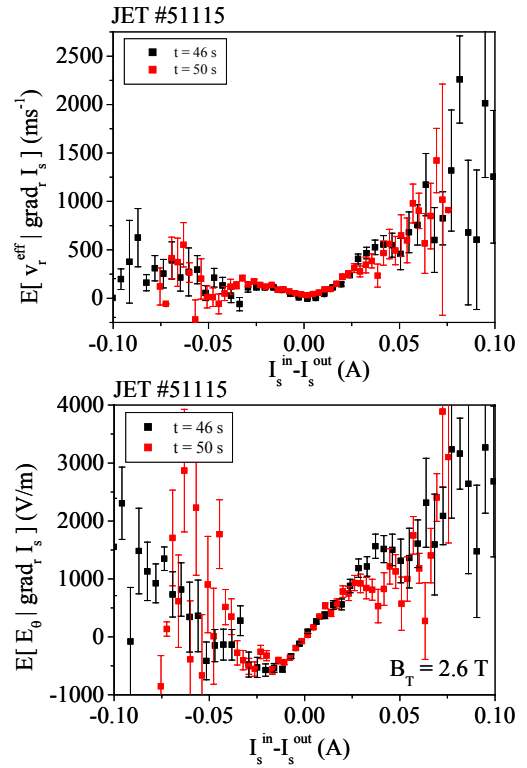


Figure 3.25(a) Effective radial velocity versus fluctuations in the radial gradient; (b) Poloidal electric fields versus radial gradient. Measurements were taken at  $r - r_{LCFS} \approx 1$  cm.

The radial structure of radial perturbations and velocities associated with ELMs has been investigated using Langmuir probe signals measured at different radial location in the SOL region. Raw data show that the size of the radial perturbation ( $\nabla \tilde{I}_s$ ) linked to ELMs decreases as

increasing the distance to the LCFS. However, experimental results show that the maximum radial speed of ELMs does not significantly depend on the distance to the LCFS [ $r - r_{LCFS} = (1 - 6)$  cm] (Figure 3.26, suggesting a ballistic rather than diffusive propagation mechanism in the SOL region.

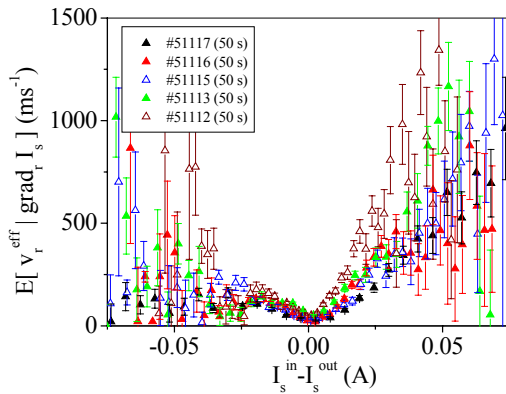


Figure 3.26 - Expected value of the radial effective velocity for a given density gradient. The maximum effective velocity and poloidal electric field linked to ELMs seems to be independent of the distance to the LCFS.

The effective radial velocity of ELM transport events in JET is rather similar to the radial velocity of ELMs previously reported in spherical tokamaks and of large transport events reported in L-mode plasmas. Interestingly this value is rather close to the speed of 200 m/s reported during the evolution of the transport profile through the L-H transition in JET. However, ELMs radial speed in the SOL is much larger than the effective radial velocity of simplified simulations of diffusive transport in the SOL region. These results suggest the existence of different transport mechanisms for small and large transport events (non-diffusive) in the JET plasma boundary region.

Mach probe measurements have shown that during the appearance of ELMs, perturbations in the ion saturation current are larger (about a factor of 3) in the probe facing the outer divertor (e.g. region of bad curvature) than in the probe facing the inner divertor (e.g. region of good curvature). This result implies that ELM events and parallel flows are dynamically linked. This result might reflect the strong ballooning character of ELMs but it also suggests that parallel flows are strongly affected by fluctuations. This conclusion is consistent with recent results in JET showing a dynamical coupling between turbulent transport events and parallel flows.

The studies show that the radial velocity of ELMs increases with the ELM size and is independent of the distance to the LCFS. ELMs arrival time to the plasma wall can be comparable to, or even smaller than, the characteristic time of transport to the divertor plates (in the range of 0.1 – 0.5 ms). In these circumstances we have to

consider the competition between parallel and radial transport of ELMs to explain and predict particle and energy fluxes onto the divertor plates in ITER. The large radial speed of ELMs might explain experimental results showing that only about 60 % of the energy losses due to large type I ELMs arrives at the divertor plates.

### 3.4. ENHANCEMENTS

#### 3.4.1. Introduction

The Association EURATOM/IST has been in charge with the tasks referred to in Table 3.4, in the frame of the JET-EP Project

#### 3.4.2. Study of Turbulence by Microwave reflectometry (JW0-OEH-IST-02/03)

##### 3.4.2.1. Introduction

The following main activities have been performed in 2002:

- Shipping to JET of the microwave and data acquisition components;
- Commissioning of the diagnostic at JET;
- Development of software for the integration of the dedicated data acquisition system in CODAS, including the adaptation of a new communication protocol;
- Supply of new analogue output boards;
- Intensive tests of the microwave components and data acquisition system;
- Elaboration of the Final Report.

##### 3.4.2.2. Operation of the upgraded reflectometer system

The old X-mode reflectometer (92-96 GHz) has been upgraded with three new channels, covering the 76-78, 85-87 and 100-106<sup>3</sup> GHz ranges (Table 3.5), for plasma turbulence studies. A dedicated VME data acquisition system (Table 3.6) as well as control programs and communication protocols have been also developed. Figure 3.27 shows a schematic of the links and connections of the upgraded reflectometer system. The configuration of the new microwave channels and the transient recorder modules are described in the “2001 Annual Report”.

All four channels are dual-frequency reflectometers, with in-phase/quadrature detection, launching one fixed frequency signal and one tuneable to measure within a variable separation of a few centimetres between the corresponding reflecting plasma layers. The variation of the correlation coefficients (between the two signals, for both phase and amplitude) with frequency separation enables to estimate a local value of the radial correlation length of the fluctuations.

<sup>3</sup> Work in collaboration with Princeton Plasma Physics Laboratory.

Name	Frame
Study of Turbulence by Microwave Reflectometry-Project Leader	JW0-OEH-IST-02
Study of Turbulence by Microwave Reflectometry	JW0-OEH-IST-03
Mw Access - Project Management and Implementation	EFDA/01-625
Real-time diagnostic	Notification
FDA Project design and procurement activities	JW2-TA-EP-FDA-01

Table 3.4 – Tasks concerning the JET-EP Project

Characteristic	Microwave systems			
	2 Oscillator		3 Oscillator	
	76-78 GHz (CFN)	85-87 GHz (CFN)	92-96 GHz (JET)	100-106 GHz (PPPL)
Output power (dBm)	13	13	11.7	14
Min. Detec. Sig. (dBm)	-80	-80		
IF Bandwidth	10MHz	10MHz	4 GHz	6 GHz
System Bandwidth	1MHz	1MHz	1MHz	1MHz
Freq. Diff. Resolution (kHz)	50	50	100	150
PLL	Yes	Yes	No	No
Leakage influence	High	High	Low	Low
Microwave offset level	High	High	Some	Low

Table 3.5 – Main features of the microwave system

Sampling freq. (kHz)	Fast ADC	DSP (RMS)	
	2000-100	16	16
Number of channel		8 channel (dc-10 kHz)	8 channel (10-250 kHz)
Memory / channel	1.5 Msample	120 ksamples	

Table 3.6 – Main features of the new acquisition system

The new reflectometer system provides at each time the correlation length at four different radial positions. Each correlation measurement is made during a plateau in which the frequency difference between the two sources of each channel is fixed. The frequency difference is then changed for the next plateau and another correlation measurement is made. After several correlation measurements it is possible to estimate the local value of the radial correlation length.

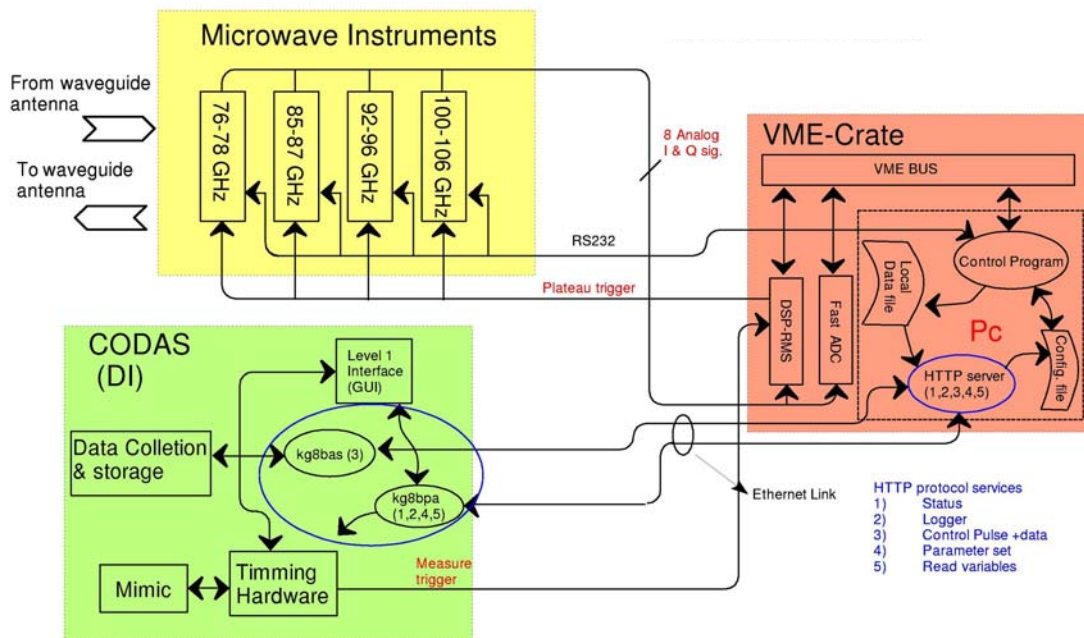


Figure 3.27 - Schematic of the links and connections of the upgraded diagnostic

### 3.4.3. Microwave Access (EFDA/01-625)

This Project aims at the installation of a new access for microwave /millimetre wave diagnostics on JET, namely for reflectometry and ECE. It consists of the installation (in-vessel and ex-vessel) of 6 waveguide runs using latest technology of corrugated waveguides and antennas for lowest loss and widest frequency range. This project has the participation of CFN-IST, IPP, FOM, CNR and the coordination is ensured by Dr. Luis Cupido (Project Leader). In 2002, the work on specification Tasks has progressed, namely:

- Elaboration of Task 1.0 report on the reflectometry frequency access range and waveguide specifications;
- Elaboration of Task 2.0 report on the antenna design specifications and performance.

### 3.4.4. Real-time diagnostic

The Portuguese EURATOM Association has been collaborating on the development of software for the real-time operation of the Motional Stark Effect diagnostic.

### 3.4.5. Fast ADC system upgrade for the heterodyne radiometer kk3 diagnostic

#### 3.4.5.1. Main activities

The following main activities were carried out:

- Design, production and test of eight FastADC modules in CFN;
- Assembling and test of the FastADC boards in a CODAS VME crate and installation in a CODAS cubicle near the KK3 diagnostic;
- Integration of the system software in the CODAS offline network and test of CODAS compliance;
- Implementation and test of a system Remote Boot feature to ease the maintenance task in the case of hardware failure by allowing readily changing the system hard disk and backup/restore the system software;
- Test of the system in the online CODAS network by acquiring real data from the JET tokamak. Collected data was analyzed and compared with the data obtained from the old system using data reduction techniques on the new data in order to allow a correct comparison. Both data sets were found to match almost perfectly showing the correct operation of the system.

#### 3.4.5.2. System description

A complete system incorporating six FastADC VME modules has been designed and was installed in the JET CODAS data acquisition system. The onsite developed digitizers (Figure 3.28) provide 48 channels with the following main characteristics:

- 6 Ms memory per channel;
- 1 Ms/s, 12 bit synchronous sampling;

- External trigger/clock/gate;
- $\pm 0.625 \text{ V}@1\text{M}\Omega$ ,  $\pm 1.25 \text{ V}@1\text{M}\Omega$ ,  $\pm 2.5 \text{ V}@1\text{M}\Omega$ ,  $\pm 5 \text{ V}@10\text{k}\Omega$  selectable, differential inputs;
- 500 kHz differential 3rd order passive anti-aliasing filter.

The integration software to JET CODAS running under Linux RedHat 7.3 was designed allowing the system to be accessed from CODAS through a Fast Ethernet link.

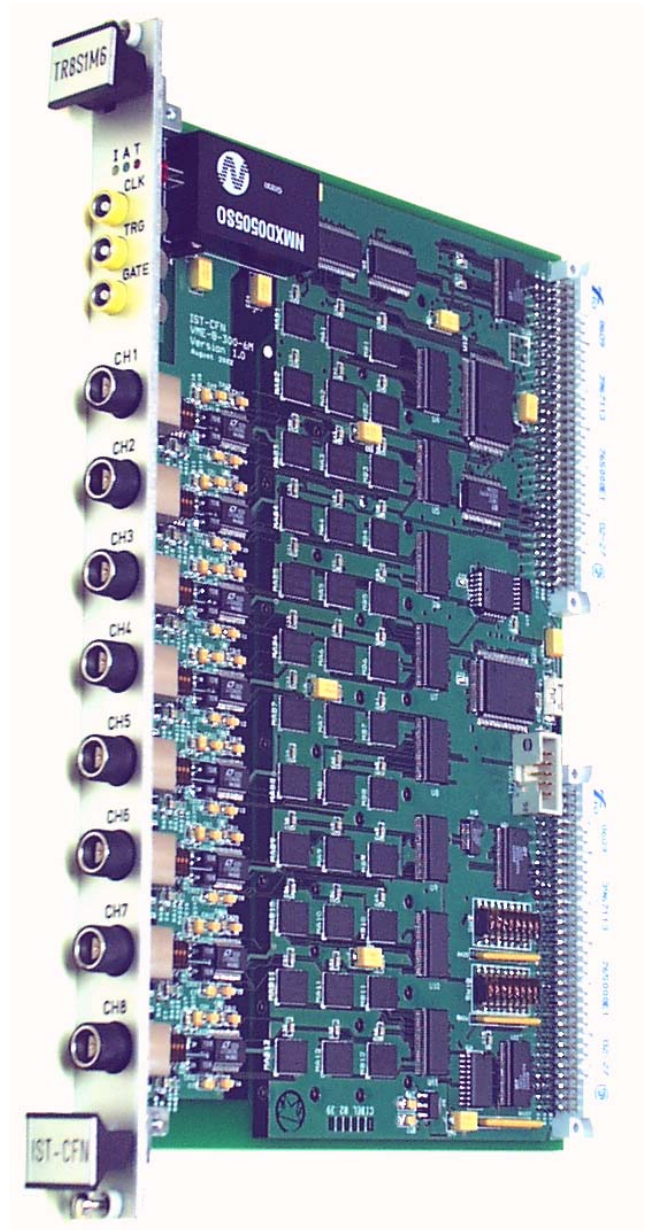


Figure 3.28 – Fast ADC Module layout.

#### **3.4.6. ICRH project**

The following main activities have been made in 2002:

- Preliminary study of the waveguides taking into account the space constraints inside the tokamak;
- Ray tracing calculations using adequate antenna patterns and typical JET plasma geometries, in order to estimate the reflectometers performance for the foreseen antenna positioning;
- Beginning of the development of the software.

#### **3.5. MANAGEMENT**

The Association EURATOM/IST has collaborated on the management of the use of the JET Facilities by the EFDA Associates in the following manner:

- Dr. Duarte Borba as a member of the staff of the Close Support Unit to the EFDA Associate Leader for JET;
- Prof. Fernando Serra as a member of the EFDA Sub-Committee for JET (until 6 March 2002) and as a member of the Scientific and Technology Advisory Committee STAC (from March 2002);
- Prof. Horácio Fernandes and Dr. Paulo Varela as members of the Remote Participation Users Group.